*Int. J. Electrochem. Sci.*, 16 **(2021)** Article ID: 210538, doi: 10.20964/2021.05.53

**International Journal of**
**ELECTROCHEMICAL**
**SCIENCE**
www.electrochemsci.org

# Synthesis of $Fe_3O_4$@C Composites Using Cellulose and Ferric Tartrate Complex as Precursor and Their Application as Anode for High Performance Lithium-Ion Batteries

*Chengmin Sun*[1,§], *Xiang Zheng*[1,§], *Tian Sun*[1,§], *Zhengguan Xu*[1], *Yapeng Yuan*[1], *Xuehua Liu*[1], *Aiping Fu*[2,3], *Hongliang Li*[1,3,*]

[1] Institute of Materials for Energy and Environment, College of Materials Science and Engineering, Qingdao University, Qingdao 266071, China
[2] College of Chemistry and Chemical Engineering, Qingdao University, Qingdao 266071, China
[3] State Key Laboratory of Biopolysaccharide Fiber Forming and Eco-Textile, Qingdao University, Qingdao 266071, China
[§] These authors contribute equally to this work
[*]E-mail: lhl@qdu.edu.cn

*Received:* 25 January 2021 / *Accepted:* 14 March 2021 / *Published:* 31 March 2021

$Fe_3O_4$ is a kind of promising anode material for lithium-ion batteries, however, the poor electrical conductivity and serious volume expansion limit their practical application in practice. In this article, the $Fe_3O_4$@C composite is prepared by facilely decomposing of the cellulose/ferric tartrate complex system. A ferric tartrate complex aqueous solution has been explored to dissolve cellulose. After a freeze-drying and subsequently carbonization at high temperature, ferric tartrate complex is decomposed to $Fe_3O_4$ and deposited homogenously inside the porous carbon derived from cellulose, obtaining the in-situ porous $Fe_3O_4$@C composites. The porous carbon can provide good electrical conductivity and adapt to the volume change of the $Fe_3O_4$ nanoparticles in electrochemical research. As LIB anode material, The $Fe_3O_4$@C anode delivers high initial charging capacity of 864.9 $mAh\cdot g^{-1}$ at 100 $mA\cdot g^{-1}$ and excellent cycling stability of 86.4% capacity retention after 300 cycles at 1000 $mA\cdot g^{-1}$.

**Keyword:** Cellulose, Ferric tartrate complex, $Fe_3O_4$@Carbon composite, Lithium-ion batteries.

## 1. INTRODUCTION

In recent years, in addition to being widely used in portable electronic devices, lithium-ion batteries have gradually begun to be used in large-scale energy storage fields such as electric vehicles and electric cruise ship[1-3]. However, the theoretical specific capacity of the traditional graphite anode is only 372 $mAh\cdot g^{-1}$, which is difficult to satisfy the needs for higher energy density lithium-ion batteries[4, 5]. With the further development of the battery field, exploiting new electrode materials with better electrochemical performance is more and more urgent.

Over the years, researchers have developed a variety of anode materials, such as transition metal oxides[6-8], silicon[9-11], and tin[12, 13]. Among them, $Fe_3O_4$ material, with the characteristics of clean, low cost and high theoretical capacity of 926mAh·g-1, is regard as a great substitute for traditional graphite anode[14,15]. Among various electrode materials, $Fe_3O_4$ is an anode material with great application potential[16,17]. However, there are also some disadvantages that limit its practical application: (1) as a semiconductor material, $Fe_3O_4$ has a low conductivity, which affects the conductivity of the anode materials[18]; (2) The formation of the solid electrolyte interphase (SEI) films will consume a great deal of lithium ions during charge/discharge process, resulting in a higher irreversible capacity and a lower Coulombic efficiency[14,19]; (3) During the cyclic process, the $Fe_3O_4$ anode displays a large volume expansion, which pulverizes the active material and induce the separation of anode materials from the current collector during the subsequent cycle[20]. As a result, the pure $Fe_3O_4$ anode material shows poor cycling performance and low specific capacity.

In order to solve these problems, researchers have adopted a variety of strategies to optimize the $Fe_3O_4$ anode materials. The mesoporous carbon material has the advantages of large specific surface area, good electrical conductivity and small volume change[21,22]. It is considered to be an ideal framework material for electrode material. Yang et al.[15] synthesized $Fe_3O_4$@C composites by a simple solvothermal method with porous three-dimensional nanostructures. The $Fe_3O_4$ nanoparticles are deposited homogenously inside the porous carbon material and displayed excellent electrochemical properties as LIB anode material. The $Fe_3O_4$@C composite anode possessed the reversible capacity of 1450 $mAh\cdot g^{-1}$ in the initial cycle and 1300 $mAh\cdot g^{-1}$ after 100 cycles. Han et al.[23] prepared $Fe_3O_4$@Carbon microsphere composites by a simple electrospray method. The abundant mesopores in the carbon matrix could effectively adapt the volume change of $Fe_3O_4$ during charging/discharging process and promote the rapid diffusion of ions. As an anode material, the composites deliver excellent reversible specific capacity of 1317$mAh\cdot g^{-1}$ and rate performance of 525$mAh\cdot g^{-1}$ at 5$A\cdot g^{-1}$. Therefore, the $Fe_3O_4$ nanoparticles in combination with mesoporous carbon material is a promising choice to improve the electrochemical performance of $Fe_3O_4$ material.

Herein, we have reported a novel approach to synthesize porous $Fe_3O_4$@C by dissolving cellulose using FeTNa (NaOH solution containing ferric tartrate complex) solution. After a freeze-drying process, the FeTNa/cellulose complex were then decomposed at high temperature in an inert atmosphere. Meanwhile, the cellulose converted into porous carbon framework while FeTNa changed to $Fe_3O_4$, resulting in porous $Fe_3O_4$@C composites. During charge/discharge processes, the porous carbon not only provides a conductive three-dimensional framework, but also offer sufficient space to relieve the volume expansion of $Fe_3O_4$ nanoparticles. As LIB anode material, the $Fe_3O_4$@C composites anode material delivers initial charging specific capacity of 864.9 $mAh\cdot g^{-1}$ at 100 $mAh\cdot g^{-1}$ and capacity retention of 617.3 $mAh\cdot g^{-1}$ at 1000$mA\cdot g^{-1}$ after 300 cycles.

## 2. EXPERIMENTAL SECTION

### *2.1 Synthesis of $Fe_3O_4$@C composites*

According to the reported method[24], FeTNa (NaOH solution containing ferric tartrate complex) solution was used to dissolve cellulose. In a typical synthesis, 7.54 g of sodium tartrate dihydrate was dissolved into 30 ml of deionized water with an ice-water bath. Then, added 2.70 g of ferric chloride hexahydrate in the solution and stirred for 30 min with magnetic stirrer. Thereafter, 47.36 ml of 2.5 $mol\cdot L^{-1}$ sodium hydroxide aqueous solution was dropped into the above solution slowly with a peristaltic pump. The dropping rate was conserved to keep the temperature of the solution below 15°C.

Cellulose was then dissolved by the above obtained FeTNa solution in a solute mass ratio of 1:X (X=0.01, 0.05 and 0.10), and three typical masses of cellulose i.e. 0.13, 0.67, and 1.41g has been applied. After cellulose is dissolved completely by the FeTNa aqueous solution, the resulted suspension was dried by freeze-drying technique and subsequently calcined at 500°C in an Ar atmosphere for 5 hours. The carbonized samples were washed with deionized water until the rinsing solution turn to neutral and then dried in vacuum oven at 60°C for 12h. Correspondingly, the as-prepared $Fe_3O_4$@C samples were denoted as $Fe_3O_4$@C-1, $Fe_3O_4$@C-5 and $Fe_3O_4$@C-10, respectively.

### *2.2 Characterization*

The morphology and elemental compositions of the samples was characterized by scanning electron microscope (SEM, JEOL-7800F). The X-ray diffraction (XRD) patterns were obtained by a Rigaku ultima IV XRD X-ray diffractometer using Cu Kα radiation. The contents of $Fe_3O_4$ and carbon in the sample were measured by thermogravimetric analysis (TGA, TG/DTA6300) from 40 to 700°C at temperature increasing step of 10°C/min under air atmosphere. The nitrogen adsorption/desorption isotherms were collected with a Quantachrome Autosorb-IQ-MP/XR. The Brunauer-Emmett-Teller method is applied to estimate the specific surface under the relative pressure range $P/P_0 = 0.05$-$0.35$ and the pore size distribution of the sample is calculated the Barrett-Joyner-Halenda model with the desorption branch data.

### *2.3 Electrochemical characterization*

The electrochemical performance of $Fe_3O_4$@C composites was characterized using 2016-type coin cells. Active material, conductive carbon black and carboxymethyl cellulose (CMC) were uniformly mixed in deionized water at a ratio of 8:1:1. The slurry was uniformly coated on copper foil and dried in the vacuum oven at 60°C for 12 hours. The coin cells were assembled in an argon atmosphere glove box using metallic lithium as the reference electrode, Celgard 2400 microporous polypropylene membrane as the separator and 1M LiPF6 dissolved in EC/DEC/DMC (1:1:1 by volume) as the electrolyte. The galvanostatic charge/discharge performance was tested on a CT2001A LAND battery test system in the voltage range of 0.1V-3.0V at the room temperature. The cyclic voltammetry tests were performed on a CHI760D electrochemical workstation at a scanning rate of $0.1 mV\cdot s^{-1}$ in the voltage range of 0.01 to

3V. The electrochemical impedance spectroscopy was recorded on the same electrochemical workstation in the frequency range from 0.001Hz to 100KHz.

## 3. RESULTS AND DISCUSSION

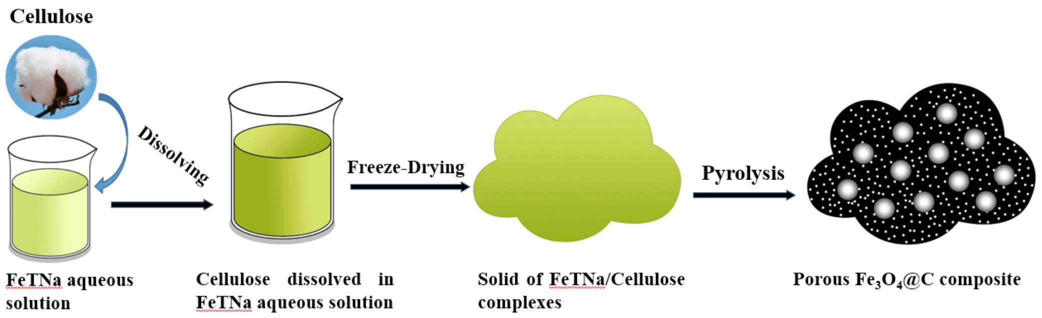

**Figure 1.** Schematic illustration of fabrication process of $Fe_3O_4$@C composites

Figure 1 shows the synthesizing method of the $Fe_3O_4$@C composites. First, use ferric tartrate complex aqueous (FeTNa) solution to dissolve cellulose. Then, after freeze-drying and subsequently carbonization at high temperature, ferric tartrate complex is decomposed to $Fe_3O_4$ and deposited homogenously inside the porous carbon material, obtaining the in-situ porous $Fe_3O_4$@C composites.

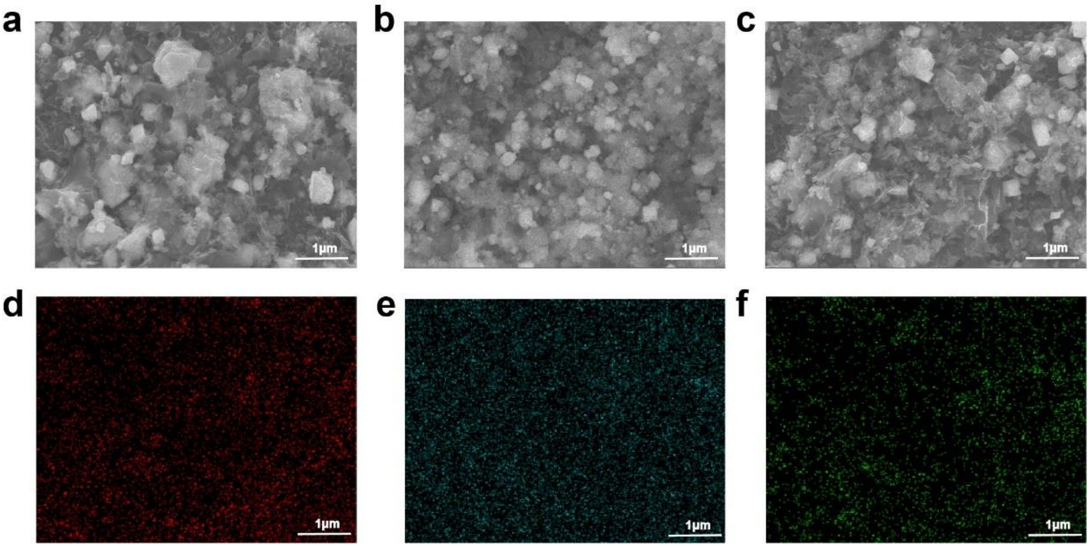

**Figure 2.** SEM images of (a) $Fe_3O_4$@C-1, (b) $Fe_3O_4$@C-5 and (c) $Fe_3O_4$@C-10. (d-f) the elemental mappings of C, Fe, O for $Fe_3O_4$@C-5

The morphology and elemental compositions of $Fe_3O_4$@C composites were characterized by scanning electron microscope (SEM). As shown in figure 2, the $Fe_3O_4$ nanoparticles were uniformly embedding in the carbon frameworks. However, in figure 2a, it was observed that several large particles with size of several hundred nanometers were incorporated in the $Fe_3O_4$@C-1 composite due to the low carbon content which can’t form a continuous supporting network, resulting in agglomeration of $Fe_3O_4$

nanoparticles. In the samples of $Fe_3O_4$@C-5 and $Fe_3O_4$@C-10 (Figure 2b and c), $Fe_3O_4$ nanoparticles could be evenly distributed in them without agglomeration. Such a characteristic of the structure can be ascribed to the formation of complexes between FeTNa and cellulose, which help to break the hydrogen bonds among the cellulose macromolecule chains and to dissolve cellulose in the aqueous solution of FeTNa. The elemental mappings of $Fe_3O_4$@C-5 composite collected with the energy dispersive spectrometer (EDS) attached on the SEM have been shown in Figure 2d, e and f. It is evident that the C, Fe and O elements are uniformly distributed in the composite, and also proved that the $Fe_3O_4$ nanoparticles were deposited homogenously inside the porous carbon.

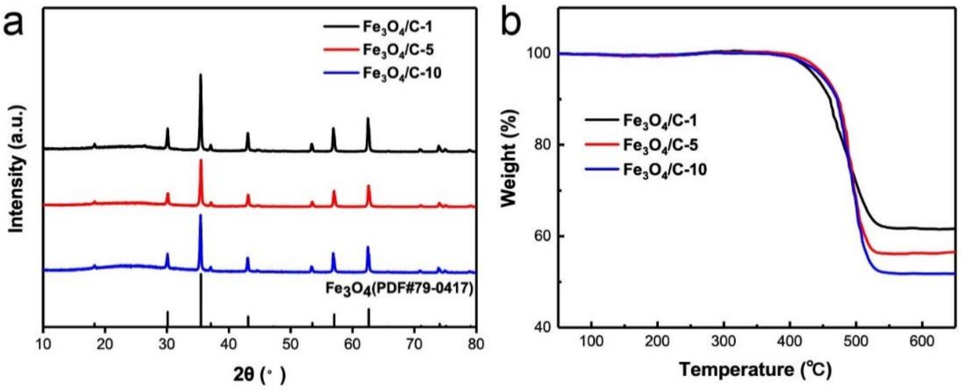

**Figure 3.** (a) XRD pattern of these $Fe_3O_4$@C composites, and (b) The TG curves of them.

Figure 3a shows the XRD patterns of the $Fe_3O_4$@C composites. From the curves, it is obvious that all the three samples show diffraction peaks at 18.3°, 31.4°, 35.5°, 43.1°, 53.5°, 57.0° and 62.6°, which can be indexed to the (220), (311), (222), (400), (422), (511) and (400) crystal planes, respectively, of $Fe_3O_4$ (JPDS No. 75-0033). The XRD results confirm the formation of the $Fe_3O_4$ compound[25]. The sharp diffraction peaks and higher intensity also demonstrate that the $Fe_3O_4$ nanoparticles are in good crystallinity. The broad diffraction peak appears at 24° corresponding to the characteristic peak of the amorphous carbon, indicating the carbon matrix of the three $Fe_3O_4$@C composites are amorphous ones[26].

The composition of the $Fe_3O_4$@C composites was characterized by thermogravimetric analysis (TGA). As shown in Figure 3b, when the temperature rose to 300°C, there is a slight mass increase which can be attributed to the oxidation of $Fe_3O_4$ to $Fe_2O_3$[27]. The quality of the samples achieved a stable equilibrium at around 540°C indicating that all the carbon moieties in the composites has been burned. Based on the TG curves, the carbon contents of 8.5wt%, 43.4wt% and 48.2wt% can be calculated in composites of $Fe_3O_4$@C-1, 5 and 10, respectively. Correspondingly, the $Fe_3O_4$ content of 61.5%, 56.6% and 51.8%, respectively, in them can be deduced. The carbon contents in these $Fe_3O_4$@C composites are proportional to the mass ratio of dissolved cellulose.

Nitrogen sorption isotherms of these $Fe_3O_4$@C composites have been tested to analyze the specific surface area and pore size of them and the results have been depicted in Figure 4. All three samples showed type IV isotherms, indicating that the composite material possess a typical mesoporous structure (see Figure 4a, c and e). With the increase of the amount of dissolved cellulose, the specific surface area is reduced gradually from 300.1 $m^3 \cdot g^{-1}$ for $Fe_3O_4$@C-1 to 183.7 for $Fe_3O_4$@C-5 and 131.4 $m^3 \cdot g^{-1}$ for $Fe_3O_4$@C-10. Carbonized cellulose will occupy part of the pores formed by rinsing off the sodium salt, causing a decrease in the specific surface area. Alternatively, low cellulose content can't form a stable carbon network, resulting in agglomeration of $Fe_3O_4$ nanoparticles, which further increases the specific surface area. All these three samples show ore size distribution in between 3-5nm as have been displayed in Figure 4b, d and f. The suitable pore structure can not only offer sufficient active sites to promote the transmission of ions and electrons, but also adapts to the volume change of the $Fe_3O_4$ active material during charging/discharging process.

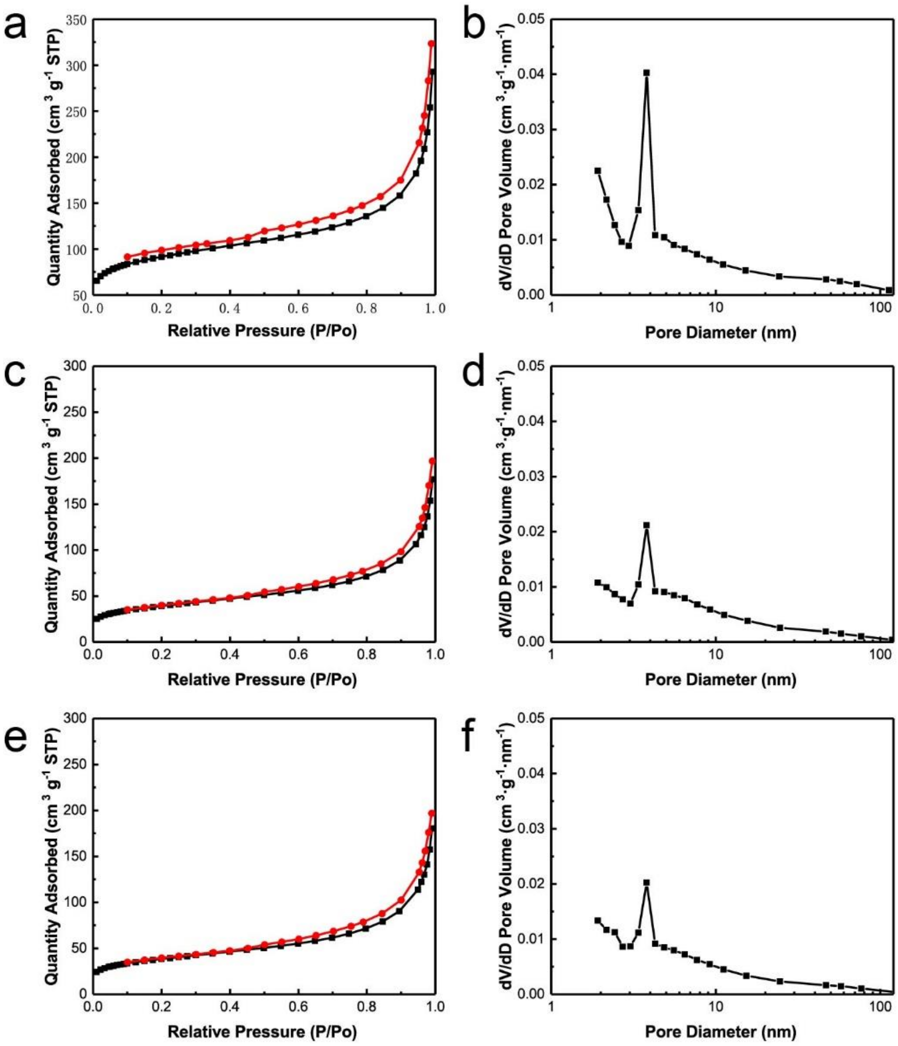

**Figure 4.** $N_2$ adsorption-desorption isotherms and pore size distribution profiles of $Fe_3O_4$-1 (a, b), $Fe_3O_4$@C-5 (c, d), and $Fe_3O_4$@C-10 (e, f).

The electrochemical performance of these $Fe_3O_4$@C composites has been evaluated in 2016-type coin cells using metallic lithium as reference electrode and the results are presented in Figure 5. The galvanostatic measurements of the $Fe_3O_4$@C composites have been carried in the voltage range of 0.01-3V at a current density of $100mA \cdot g^{-1}$ (Figure 5a). From the first discharge curve, an obvious voltage plateau at 0.75V can be corresponded to the reduction of $Fe_3O_4$ to Fe. The first discharge/charge specific capacity of the $Fe_3O_4$@C-1, 5 and 10 composites are 1328.6/899.1, 1263.7/864.9 and 1100.9/757.5mAh·$g^{-1}$, corresponding the initial Coulombic efficiency is 67.67%, 68.44% and 68.81%, respectively. With the increase of carbon concentration, it is apparent that the capacity of the $Fe_3O_4$@C composites decreases gradually because of the specific capacity of carbon material is much lower than $Fe_3O_4$.

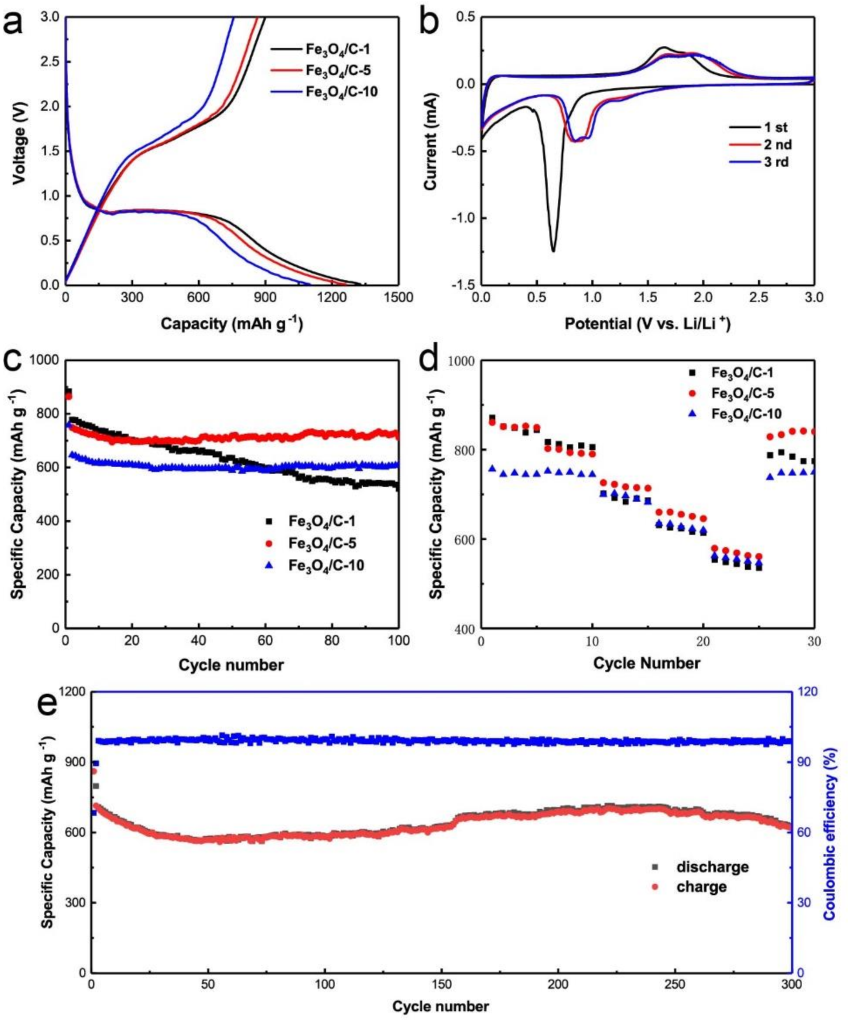

**Figure 5.** (a) first voltage profiles, (b) CV curves for the first three cycles of $Fe_3O_4$@C-5 composite, (c) cycling performance of the three $Fe_3O_4$@C composites, (d) rate performance, and (e) cycles and Coulombic efficiency for $Fe_3O_4$@C-5 sample at 1000 mA $g^{-1}$

The irreversible lithium loss in the charge/discharge process is ascribed to the formation of solid electrolyte interface (SEI) and the abundant mesoporous structure irreversibly capturing lithium ions. Furthermore, the cyclic voltammograms (CVs) tests for the $Fe_3O_4$@C-5 composite with a scan rate of 0.1mV/s and voltage in between 0.01V and 3V have been conducted and the first three cycles are shown in Figure 5b. In the first cycle process, an obvious reduction peak appearing at 0.65V can be ascribed to the formation of SEI. In the subsequent cycle, the reduction peak shifted to 0.9V corresponding to the reduction of $Fe_3O_4$ to metallic Fe and the formation of $Li_2O$ ($Fe_3O_4 + 8Li^+ + 8e^- \rightarrow 3Fe + 4Li_2O$) [28]. The oxidation peaks appeared at 1.6 and 1.8V is corresponding to the conversion reaction of Fe to $Fe_3O_4$ [29]. The obvious shift of reduction and oxidation peaks indicated that the structure has been significantly changed[30]. The CV curves of the subsequent cycle show good consistency, which also means that the batteries possess excellent cycle stability.

The cycling stability of these $Fe_3O_4$@C composites at 500 $mAh \cdot g^{-1}$ for 100 cycles were presented in Figure 5c. With the decreases of carbon content, the cycle stability of the $Fe_3O_4$@C composites is going down gradually. Although the first charge specific capacity of the $Fe_3O_4$@C-1 anode has the highest capacity of 777.7$mAh \cdot g^{-1}$, the retention rate was only 58.9% after 100 cycles. The rapid dropping of capacity can be ascribed to the low content of carbon in the composite, which can't construct a stable conductive framework and suppress the huge volume change of $Fe_3O_4$ nanoparticles [31,32]. In contrast, the $Fe_3O_4$@C-10 composite exhibited excellent cycling stability, even though the first discharge capacity of the sample is only 646.6$mAh \cdot g^{-1}$ due to the low content of $Fe_3O_4$. In comparison with the other two samples, the $Fe_3O_4$@C-5 sample possesses better comprehensive performance. The results have shown that the $Fe_3O_4$@C-5 anode has the high specific capacity of 749.3$mAh \cdot g^{-1}$ and great cycle stability with 96.9% capacity retention after 100 cycles.

Figure 5d displayed the rate capability of the $Fe_3O_4$@C composites at the current density from 100 to 2000 $mA \cdot g^{-1}$. It was obvious that all the three composites show outstanding rate performance. In particular, the $Fe_3O_4$@C-5 composite exhibits the best performance of 861.0, 802.4, 726.1, and 660.2 $mAh \cdot g^{-1}$ at the current density ranges from 100 to 2000$mA \cdot g^{-1}$, respectively. Even after going through high-rate cycling, the capacity of the samples can restore to initial levels when the rate returns to 100$mA \cdot g^{-1}$. The reason of the excellent rate performance is because of the porous carbon matrix which establishes the fast ion/electron transmission channels and provide stable conductive networks to maintain favorable electrical contact between active material and current collector. Taking into consideration the comprehensive performance, the long-term cyclability of $Fe_3O_4$@C-5 anode was further examined under 1000$mA \cdot g^{-1}$ in Figure 5e. It is found that the first discharge specific capacity is 714.2$mA \cdot g^{-1}$ and still remains at 617.3$mA \cdot g^{-1}$ corresponding to 86.4% capacity retention even after 300 cycles. Such good properties can be explained due to the uniformly distribution of the $Fe_3O_4$ nanoparticles a in the porous carbon skeleton, which can effectively pave side effect of volume expansion of $Fe_3O_4$ nanoparticles during the cycle process.

The electrochemical impedance spectroscopy of $Fe_3O_4$@C composites has been tested to learn more properties of these composites. The Nyquist diagram as showed in Figure 6a is composed of a semicircle in the high-frequency range and an oblique straight line in the low-frequency range, which are corresponding to the charge transfer resistance ($R_{ct}$) and the diffusion characteristics of lithium ions in solid materials ($Z_w$), respectively [33]. In order to get a more intuitive result, equivalent fitting has been made using the equivalent circuit diagram as shown in Figure 6b. According to the fitting results, $Fe_3O_4$@C-1 shows a high $R_{ct}$ (43.7Ω), while $Fe_3O_4$@C-5 and $Fe_3O_4$@C-10 which dissolve a certain amount of cellulose decreased to 36.6 and 30.2Ω. It is obvious that the formation of a more uniform conductive network by dissolving more cellulose precursor could significantly reduce the resistance of the composite [34]. At the same time, the straight slope of the $Fe_3O_4$@C-5 and $Fe_3O_4$@C-10 materials in the low frequency region are higher than $Fe_3O_4$@C-1, which means that they own a faster $Li^+$ diffusion rate than the latter. It is also consistent with the carbon contents in them.

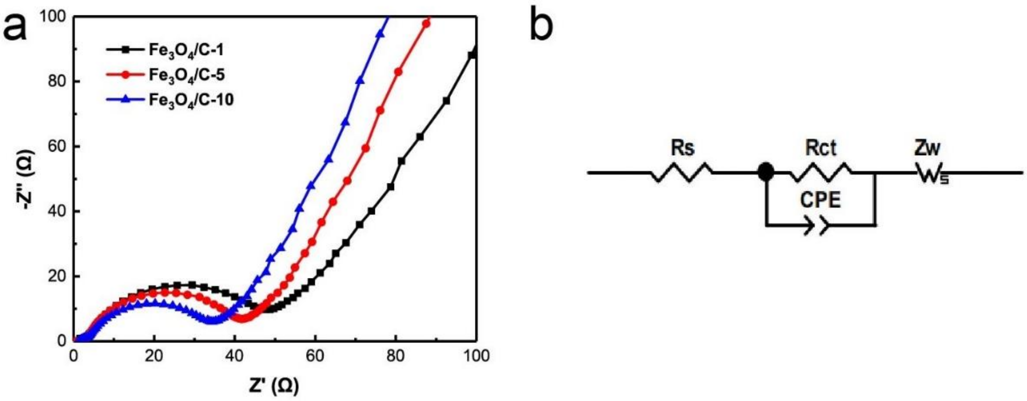

**Figure 6.** (a) The EIS spectra of these $Fe_3O_4$@C composites, and (b) the equivalent circuit

The electrochemical performance of the similar $Fe_3O_4$ composites described in previous literatures are shown in Table 1. By contrast, it is clear that the $Fe_3O_4$ composites in this work exhibit better rate performance and cycle performance. Obviously, the stable carbon network formed by pyrolyzing the dissolved cellulose can increase the electronic conductivity of the resulted $Fe_3O_4$@C composites and improve the electrochemical performance of them.

**Table 1.** Comparison of electrochemical performance of different $Fe_3O_4$ composites

| **Composites** | **Rate performance** | | **Cycle performance** | | | **Ref.** |
|---|---|---|---|---|---|---|
| | Capacity (mAh·g$^{-1}$) | Current density (mA • g$^{-1}$) | Final capacity (mAh·g$^{-1}$) | Current density (mA • g$^{-1}$) | Cycle | |
| $Fe_3O_4$ nanospheres | 631 | 2000 | 743 | 200 | 100 | [17] |
| $Fe_3O_4$@C | 150 | 1000 | 539 | 100 | 100 | [19] |
| $Fe_3O_4$@C | 545 | 2000 | 525 | 1000 | 300 | [23] |
| $Fe_3O_4$@C nanofibers | 636 | 1000 | 611 | 1000 | 300 | [27] |
| $Fe_3O_4$@C nanosheets | 309 | 1000 | 647 | 100 | 100 | [35] |
| $Fe_3O_4$ nanoparticles | 435 | 2000 | 522 | 100 | 200 | [36] |
| $Fe_3O_4$@C | 225 | 1600 | 522 | 100 | 100 | [37] |
| $Fe_3O_4$@C | 660 | 2000 | 617 | 1000 | 300 | This work |

## 4. CONCLUSION

$Fe_3O_4$@C composites have been successfully synthesized by using FeTNa aqueous solution to dissolve cellulose and then to decompose them at high temperature after freeze-drying of the solution. This method achieves homogenous distribution of $Fe_3O_4$ nanoparticles in the porous carbon material, which provides more active sites to promotes ion/electron transmission and adapts the volume change of $Fe_3O_4$ nanoparticles during charging/discharging process. As LIB anode material, the $Fe_3O_4$@C anode exhibits high reversible specific capacity of 864.9 $mAh\cdot g^{-1}$ at 100 $mAh\cdot g^{-1}$, outstanding rate performance, and capacity retention of 617.3 $mAh\cdot g^{-1}$ at 1000$mA\cdot g^{-1}$ after 300 cycles. A stable carbon network by dissolving more cellulose can greatly increase its electronic conductivity of the resulted $Fe_3O_4$@C composites and improve the electrochemical capability of them. This approach provides a novel method for fabrication of $Fe_3O_4$@C with superior performance and promising practical application for the future lithium-ion batteries.

ACKNOWLEDGEMENTS
This work is supported by Natural Science Foundation of Shandong Province (ZR2020ME057), the Double First Class University Construction of Shandong Province and the Taishan Scholars Advantageous and Distinctive Discipline Program of Shandong Province for supporting the research team of energy storage materials.

## References

1. V. Etacheri, R. Marom, R. Elazari, G. Salitra, D. Aurbach, *Energy Environ. Sci.*, 4 (2011) 3243.
2. T. Kim, W. Song, D.-Y. Son, L.K. Ono, Y. Qi, *J. Mater. Chem. A*, 7 (2019) 2942.
3. X. Wang, *Int. J. Electrochem. Sci.*, 16 (2021) 151011
4. S. Chae, S.H. Choi, N. Kim, J. Sung, J. Cho, *Angew. Chem., Int. Ed*., 59 (2020) 110.
5. T. Wang, X. Yu, M. Fan, Q. Meng, Y. Xiao, Y.-X. Yin, H. Li, Y.-G. Guo, *Chem. Commun.*, 56 (2020) 245.
6. Z. Li, X. Hu, Z. Shi, J. Lu, Z. Wang, *Appl. Surf. Sci.*, 531 (2020) 147290.
7. Z. Wang, L. Zhou, X.W. Lou, *Adv. Mater.*, 24 (2012) 1903.
8. H. Xue, Y. Wu, Y. Zou, Y. Shen, G. Liu, Q. Li, D. Yin, L. Wang, J. Ming, *Adv. Funct. Mater*., 30 (2020) 1910657.
9. J. Lee, J. Moon, S.A. Han, J. Kim, V. Malgras, Y.U. Heo, H. Kim, S.M. Lee, H.K. Liu, S.X. Dou, Y. Yamauchi, M.S. Park, J.H. Kim, *ACS Nano*, 13 (2019) 9607.
10. Q. Xu, J.-Y. Li, J.-K. Sun, Y.-X. Yin, L.-J. Wan, Y.-G. Guo, *Adv. Energy Mater*, 7 (2017) 1601481.
11. M.Y. Yan, G. Li, J. Zhang, Y.F. Tian, Y.X. Yin, C.J. Zhang, K.C. Jiang, Q. Xu, H.L. Li, Y.G. Guo, *ACS Appl. Mater. Interfaces*, 12 (2020) 27202.
12. J. Hassoun, G. Derrien, S. Panero, B. Scrosati, Adv. Mater., 20 (2008) 3169.
13. Z. Kong, X. Liu, T. Wang, A. Fu, Y. Li, P. Guo, Y.-G. Guo, H. Li, X.S. Zhao, *Appl. Surf. Sci*., 479 (2019) 198.
14. Z. Liu, L. Liu, Z. Zhao, J. He, S. Wang, C. Xiong, *Appl. Surf. Sci*., 526 (2020) 146639.
15. Z. Yang, D. Su, J. Yang, J. Wang, *J. Power Sources*, 363 (2017) 161.
16. R. Chu, D. Tan, J. Zhang, Y. Chen, H. Jiang, J. Lin, L. Li, Y. Zhang, H. Guo, *J. Alloys Compd*., 835 (2020) 155192.
17. H. Zhang, Int. *J. Electrochem. Sci*., 15 (2020) 4789.
18. J. Su, M. Cao, L. Ren, C. Hu, *J. Phys. Chem. C*, 115 (2011) 14469.

19. H. Lv, Int. *J. Electrochem. Sci.*, 15 (2020) 2157
20. E. Kang, Y.S. Jung, A.S. Cavanagh, G.-H. Kim, S.M. George, A.C. Dillon, J.K. Kim, J. Lee, *Adv. Funct. Mater.*, 21 (2011) 2430.
21. J. Li, R. Yao, J. Bai, C. Cao, *ChemPlusChem*, 78 (2013) 797.
22. Y. Zhai, Y. Dou, D. Zhao, P.F. Fulvio, R.T. Mayes, S. Dai, *Adv. Mater*, 23 (2011) 4828.
23. W. Han, X. Qin, J. Wu, Q. Li, M. Liu, Y. Xia, H. Du, B. Li, F. Kang, *Nano Res.*, 11 (2017) 892.
24. H. Vu-Manh, H.B. Öztürk, T. Bechtold, Carbohydrate Polymers, 82 (2010) 761.
25. J. Luo, J. Liu, Z. Zeng, C.F. Ng, L. Ma, H. Zhang, J. Lin, Z. Shen, H.J. Fan, *Nano Lett*, 13 (2013) 6136.
26. J. Liu, X. Xu, R. Hu, L. Yang, M. Zhu, *Adv. Energy. Mater*., 6 (2016) 1600256.
27. Q. Wu, R. Zhao, X. Zhang, W. Li, R. Xu, G. Diao, M. Chen, *J. Power Sources*, 359 (2017) 7.
28. C. He, S. Wu, N. Zhao, C. Shi, E. Liu, J. Li, ACS Nano, 7 (2013) 4459.
29. X. Qin, H. Zhang, J. Wu, X. Chu, Y.-B. He, C. Han, C. Miao, S. Wang, B. Li, F. Kang, *Carbon*, 87 (2015) 347.
30. P. Lian, X. Zhu, H. Xiang, Z. Li, W. Yang, H. Wang, *Electrochimica Acta*, 56 (2010) 834.
31. D. Liu, Z. Kong, X. Liu, A. Fu, Y. Wang, Y-G. Guo, P. Guo, H. Li, X. S. Zhao, *ACS Appl. Mater. & Inter.*, 10 (2018) 2515.
32. T. Liang, X. Liu, X. Liu, X. Guan, C. Wang, A. Fu, Y. Li, P. Guo, H. Li, *Energy Technol.*, 6 (2018) 2036.
33. X. Liu, X. Liu, B. Sun, H. Zhou, A. Fu; Y. Wang, Y.-G. Guo, P. Guo, H. Li, *Carbon*, 130 (2018) 680.
34. J. Liu, A. Fu, Y. Wang, P. Guo, H. Feng, H. Li, X. S. Zhao, *ChemElectroChem*, 4 (2017) 2027.
35. Q. Xin, L. Gai, Y. Wang, W. Ma, H. Jiang, Y. Tian, *J. Alloys Compd.*, 691 (2017) 592.
36. L. Guo, H. Sun, C. Qin, W. Li, F. Wang, W. Song, J. Du, F. Zhong, Y. Ding, *Appl. Surf. Sci.*, 459 (2018).
37. X. X. Yang, J. Qiu, *Mater. Res. Express*, 5 (2018) 095504.